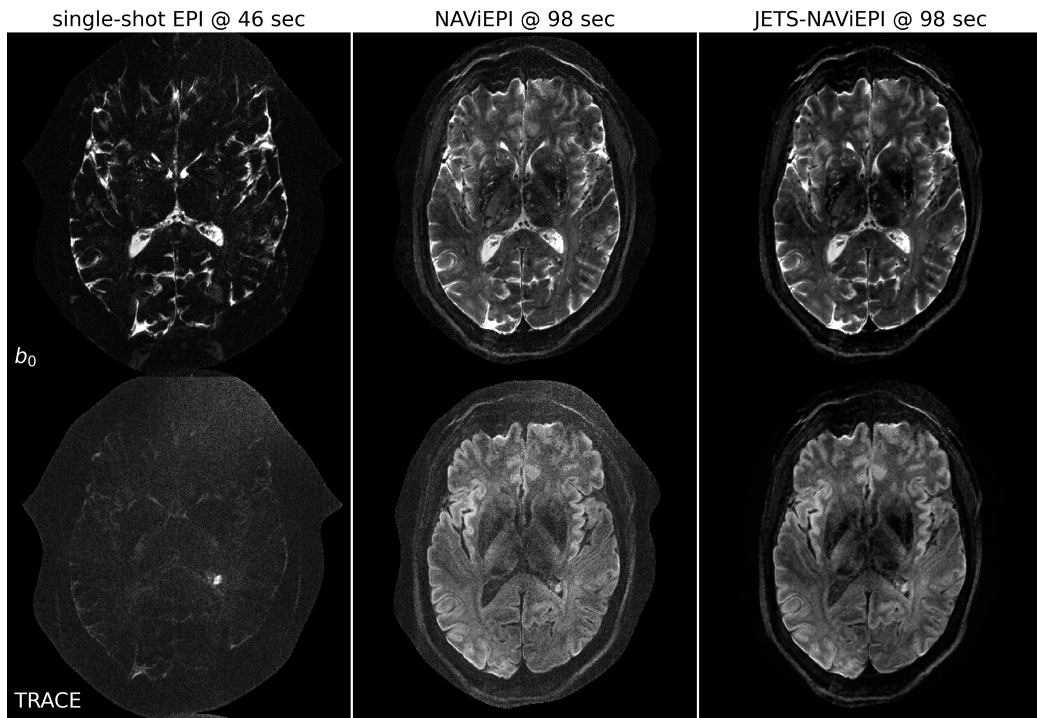


## Graphical Abstract

### Accelerated Diffusion Weighted Magnetic Resonance Imaging at 7 T: Joint Reconstruction for Shift-Encoded Navigator-based Interleaved Echo Planar Imaging (JETS-NAViEPI)

Zhengguo Tan, Patrick Alexander Liebig, Robin Martin Heidemann, Frederik Bernd Laun, Florian Knoll

**3-scan trace acquisition with voxel size 0.5 X 0.5 X 2.0 mm<sup>3</sup>**



## Highlights

### **Accelerated Diffusion Weighted Magnetic Resonance Imaging at 7 T: Joint Reconstruction for Shift-Encoded Navigator-based Interleaved Echo Planar Imaging (JETS-NAViEPI)**

Zhengguo Tan, Patrick Alexander Liebig, Robin Martin Heidemann, Frederik Bernd Laun, Florian Knoll

- Navigator-based interleaved EPI acquisition with minimal distortion mismatch between echoes
- Novel accelerated diffusion acquisition with shifted phase encoding among diffusion directions for complementary  $k$ - $q$ -space sampling at 7 T
- Generalized joint  $k$ - $q$ -slice diffusion-weighted image reconstruction with overlapping locally low-rank regularization
- Efficient simultaneous multi-slice (SMS) image reconstruction
- 3-scan trace acquisition with the voxel size  $0.5 \times 0.5 \times 2.0 \text{ mm}^3$  and 60 slices at 1.5 min

# Accelerated Diffusion Weighted Magnetic Resonance Imaging at 7 T: Joint Reconstruction for Shift-Encoded Navigator-based Interleaved Echo Planar Imaging (JETS-NAViEPI)

Zhengguo Tan<sup>a</sup>, Patrick Alexander Liebig<sup>b</sup>, Robin Martin Heidemann<sup>b</sup>,  
Frederik Bernd Laun<sup>c</sup>, Florian Knoll<sup>a</sup>

<sup>a</sup>*Department Artificial Intelligence in Biomedical Engineering (AIBE),  
Friedrich-Alexander University of Erlangen-Nuremberg, Erlangen, Germany*

<sup>b</sup>*Siemens Healthcare GmbH, Erlangen, Germany*

<sup>c</sup>*Institute of Radiology, University Hospital Erlangen, Friedrich-Alexander University of Erlangen-Nuremberg, Erlangen, Germany*

---

## Abstract

The pursuit of high spatial-angular-temporal resolution for in vivo diffusion-weighted magnetic resonance imaging (DW-MRI) at ultra-high field strength (e.g., 7 T) is important in understanding brain microstructure and function. Such pursuit, however, faces several technical challenges. First, increased off-resonance and shorter  $T_2$  relaxation require faster echo train readouts. Second, existing high-resolution DW-MRI techniques usually employ in-plane fully-sampled multi-shot EPI, which not only prolongs the scan time but also induces a high specific absorption rate (SAR) at 7 T. To address these challenges, we develop in this work navigator-based interleaved EPI (NAViEPI) which enforces consistent bandwidth between the imaging and the navigator echo. First, NAViEPI renders no distortion mismatch between the two echoes, and thus simplifies shot-to-shot phase variation correction. Second, NAViEPI allows for a large number of shots (e.g. > 4) with undersampled

iEPI acquisition, thereby rendering clinically-feasible high-resolution sub-millimeter protocols. To retain signal-to-noise ratio (SNR) and to reduce undersampling artifacts, we develop the  $k_y$ -shift encoding among diffusion encodings to explore complementary  $k$ - $q$ -space sampling. Moreover, we develop a novel joint reconstruction with overlapping locally low-rank regularization generalized to multi-band multi-shot acquisition at 7 T (dubbed JETS-NAViEPI). R1.6

*Keywords:* Diffusion-weighted magnetic resonance imaging, Echo planar imaging, Navigator, Ultra-high field, Joint reconstruction, Low rank, Simultaneous multi slice

---

<sup>1</sup> **1. Introduction**

<sup>2</sup> Diffusion-weighted magnetic resonance imaging (DW-MRI) ([Le Bihan et al., 1986; Merboldt et al., 1985](#)) is a non-invasive modality that is sensitive to the intravoxel Brownian motion of water molecules. DW-MRI forms the basis for diffusion tensor imaging (DTI) ([Basser et al., 1994; Mori et al., 1999](#)) and high angular resolution diffusion imaging (HARDI) ([Tuch et al., 2002](#)), and has been widely used in acute brain ischemia diagnosis, in tumor detection and staging, and in neuroscience ([Jones, 2010](#)).

<sup>9</sup> For DW-MRI acquisition, the commonly used pulse sequence is single-shot echo-planar imaging (SS-EPI) ([Mansfield, 1977](#)). SS-EPI is capable of rapidly acquiring one DW image per radio-frequency excitation at the order of 100 ms, and is thus motion robust. However, conventional SS-EPI, even with three-fold accelerated acquisition ([Bammer et al., 2001](#)) using parallel imaging ([Roemer et al., 1990; Ra and Rim, 1993; Pruessmann et al., 1999; Griswold et al., 2002](#)), still suffers from low spatial resolution and geometric distortions.

<sup>17</sup> In the quest for high spatial-angular-temporal-resolution and minimal-geometrical-distortion DW-MRI, tremendous efforts have been made. Techniques R3.7,  
<sup>18</sup> on the correction of image distortion induced by off-resonance and eddy currents have been developed ([Andersson et al., 2003](#)). Furthermore, gSlider R3.8  
<sup>19</sup> ([Setsompop et al., 2018](#)) with blipped-CAIPI ([Setsompop et al., 2012](#)) for simultaneous multi-slice (SMS) ([Maudsley, 1980; Breuer et al., 2005](#)) was proposed to achieve high-resolution DW-MRI. Advanced pulse sequences based R3.15  
<sup>20</sup> on multi-shot EPI have also been developed, including but not limited to interleaved EPI ([iEPI, 1993](#)), PROPELLER ([Pipe et al., 2002](#)),

26 and readout-segmented EPI (rsEPI) ([Porter and Heidemann, 2009](#); [Heide-  
27mann et al., 2010](#)).

28 Based on four-shot iEPI, multiplexed sensitivity encoding (MUSE) image  
29 reconstruction achieved DW-MRI with a sub-millimeter in-plane resolution  
30 and maximal  $b$ -value  $800\text{ s/mm}^2$  at 3 T ([Chen et al., 2013](#)). The four-shot  
31 iEPI employed in MUSE acquired an in-plane fully-sampled  $k$ -space, except  
32 partial Fourier. Every shot (segment), corresponding to four-fold under-  
33 sampling, was then reconstructed via parallel imaging to obtain shot-to-shot  
34 phase variation. This indicates that increasing the number of shots in MUSE  
35 will result in higher undersampling per shot, and consequently, degrade shot  
36 phase estimation ([Wu and Miller, 2017](#)). On the other hand, the use of in-  
37 plane fully-sampled four-shot iEPI is challenging at ultra-high field (e.g. 7 T),  
38 because the SAR is linearly proportional to the square of the field strength.

39 Alternatively, navigator-based iEPI acquisition has been proposed ([Jeong](#)  
40 [et al., 2013](#); [Dai et al., 2017, 2018](#)). These proposals may allow for a larger  
41 number of shots, and hence higher spatial resolution. However, due to the  
42 use of different bandwidth between the imaging echo and the navigator echo,  
43 these proposals suffered from geometric distortion mismatch between the  
44 two echoes and thus required specific compensation methods. In contrast,  
45 rsEPI ([Porter and Heidemann, 2009](#); [Heidemann et al., 2010](#)) used the same  
46 readout segment for both echoes, and thus required no correction of the  
47 navigator echo.

48 Beyond the MUSE-type parallel imaging reconstruction, compressed sens-  
49 ing ([Lustig et al., 2007](#); [Block et al., 2007](#)) has been explored. For instance,  
50 multi-shot reconstruction techniques based on structured low-rank matrix

51 completion (MUSSELS) (Mani et al., 2017; Bilgic et al., 2019) achieved 5-  
52 shot DW-MRI with 9-fold undersampling per shot. Recently, JULEP (Dai  
53 et al., 2023) incorporated explicit phase mapping into MUSSELS. These re-  
54 construction techniques, i.e., MUSE, MUSSELS and JULEP, targeted the  
55 reconstruction of one DW image from interleaved EPI acquisition, and did  
56 not explore joint- $k$ - $q$ -space undersampling or reconstruction.

57 Joint- $k$ - $q$ -space undersampling can be achieved via proper regularization  
58 along the diffusion encoding direction. Relevant examples are diffusion un-  
59 dersampling with Gaussian process estimated reconstruction (DAGER) (Wu  
60 et al., 2019) and magnitude-based spatial-angular locally low-rank regular-  
61 ization (SPA-LLR) (Hu et al., 2020). However, DAGER addressed the recon- R1.2,  
62 struction problem of single-shot EPI acquisition. SPA-LLR focused on the R1.10  
63 reconstruction of single-band and fully-sampled iEPI acquisition.

64 In this work, we propose a Joint  $k$ - $q$ -slice rEconsTruction framework  
65 for Shift-encoded NAVigator-based interleaved EPI at 7 T (dubbed JETS-  
66 NAViEPI). Our pulse sequence, NAViEPI, differs from most existing tech-  
67 niques. First, NAViEPI builds upon interleaved EPI, thereby allowing for  
68 fast and efficient  $k$ -space coverage. Second, inspired by rsEPI, NAViEPI  
69 ensures the same bandwidth between the imaging and the navigator echo,  
70 thereby minimizing geometric distortion and allowing for the use of a larger  
71 number of shots. NAViEPI essentially integrates the advantages of both iEPI  
72 and rsEPI. Third, NAViEPI utilizes undersampled multi-shot iEPI, thereby  
73 alleviating the SAR problem at 7 T. Fourth, NAViEPI shifts the  $k$ -space in-  
74 plane sampling pattern along the phase encoding ( $k_y$ ) direction. This shifting  
75 creates complementary  $k$ - $q$ -space sampling, which leads to the possibility of

<sup>76</sup> our joint  $k$ - $q$ -slice reconstruction. Specifically, we employ spatial-diffusion  
<sup>77</sup> overlapping LLR regularization to jointly reconstruct all diffusion encodings  
<sup>78</sup> and multi-band slices. In vivo experiments at 7 T and comparisons with other  
<sup>79</sup> techniques demonstrate the efficiency of our proposed method in achieving  
<sup>80</sup> high spatiotemporal resolution DW-MRI at ultra-high field.

81 **2. Materials and methods**

82 *2.1. Multi-band shift-encoded iEPI acquisition*

83 Fig. 1 (A) displays diffusion-weighted image acquisition based on three-  
84 shot interleaved EPI with three-fold in-plane undersampling. Conventionally,  
85 such a sampling pattern is repeated for all diffusion directions. In contrast,  
86 we propose the  $k_y$ -shifted diffusion encoding, as shown in Fig. 1 (B). The  
87 interleaved EPI sampling pattern is shifted by one  $k_y$  line per diffusion di-  
88 recton, with the cycling period being the in-plane undersampling factor.

89 It is worth noting that, as shown in Fig. 1 (A), the undersampling factor of  
90 one segment is  $R_{\text{in-plane}} \times N_{\text{shot}}$ , yielding nine-fold in-plane undersampling in  
91 this example. In other words, the undersampling factor per segment linearly  
92 scales up with the number of shots. Consequently, conventional self-gating re-  
93 construction techniques, e.g. MUSE, suffer from degraded shot-to-shot phase  
94 estimation, which in turn limits the number of shots and spatial resolution.

95 *2.2. NAViEPI: Navigator-based iEPI with consistent bandwidth between the*  
96 *imaging and the navigator echo - where iEPI meets rsEPI*

97 Instead of conventional MUSE with in-plane fully-sampled iEPI and a lim-  
98 ited number of shots, We propose NAVigator-based interleaved EPI (NAViEPI)  
99 in this work. Moreover, inspired by rsEPI ([Porter and Heidemann, 2009](#)),  
100 NAViEPI enforces a consistent bandwidth between the imaging and the nav-  
101 igitator echo, thereby minimizing distortion mismatch between the two echoes.

102 *2.3. In vivo acquisition protocols*

103 We implemented multiple in-vivo acquisition protocols at a clinical 7 T  
104 MR system (MAGNETOM Terra, Siemens Healthineers, Erlangen, Ger-

105 many) equipped with a 32-channel head coil (Nova Medical, Wilmington,  
106 MA, USA) and the XR-gradient system (maximum gradient strength 80 mT/m  
107 with a peak slew rate of 200 T/m/s). To calibrate coil sensitivity maps, refer- R3.22  
108 ence scans employed a gradient-echo (GRE) sequence. Spectral fat saturation  
109 and mono-polar diffusion-encoding gradients were used. The phase-encoding  
110 direction was selected as anterior-to-posterior.

111 This study was approved by the local ethics committee. Three volunteers R3.1  
112 with informed consent obtained before scanning participated in this study.  
113 Detailed acquisition protocols are listed in Table 1.

Table 1: NAViEPI acquisition protocols

Protocol	1.0 mm isotropic		sub-millimeter	
	#1	#2	#3	#4
Diffusion mode	MDDW <sup>1</sup>		3-scan trace	
Diffusion scheme	monopolar			
Diffusion direction	20		3	
b-value (s/mm <sup>2</sup> )	1000			
Voxel size (mm <sup>3</sup> )	1.0		0.5 × 0.5 × 2.0	
Slices	141		60	
FOV (mm <sup>2</sup> )	200		220	
Base resolution	200		440	
Navigator	No	Yes	Yes	No
Shots	4	3	5	1
TR (ms)	7700	7600	4400	8000
TEs (ms)	67	58/78	58/95.1	143
Echo spacing (ms)	1.02	1.08	1.52	1.48
Bandwidth (Hz/Pixel)	1086		758	
Partial Fourier	6/8			
Acceleration <sup>2</sup>	1 × 3	3 × 3	3 × 2	
TA (min) <sup>3</sup>	10 : 42	8 : 02	1 : 38	0 : 46

<sup>1</sup> MDDW: Multi-direction diffusion weighting;<sup>2</sup> Acceleration: Both in-plane and slice undersampling were employed, denoted as ( $R_{\text{in-plane}} \times R_{\text{slice}}$ ). For instance, 3 × 2 means 3-fold in-plane undersampling and multi-band factor 2;<sup>3</sup> TA: Total acquisition time.

115    2.3.1. 20-diffusion-direction acquisition at  $1.0 \text{ mm}^3$  isotropic resolution

116    As listed in Table 1, Protocol #1 with six-shot iEPI and without in-  
117    plane undersampling was implemented. This protocol represents the acquisi-  
118    tion scheme employed in many existing multi-shot reconstruction techniques,  
119    (e.g., MUSE, SPA-LLR, and JULEP). The acquired data from this protocol R1.1,  
120    served as ground truth. Different reconstruction methods, i.e., JETS, MUSE, R1.2  
121    and JULEP were compared.

122    We then retrospectively reduced the four-shot data to only one shot per R1.1  
123    diffusion encoding without and with the proposed  $k_y$  shifting to simulate  
124    three-fold in-plane undersampling. JETS reconstruction was performed on  
125    all data to validate the proposed  $k_y$ -shifted acquisition.

126    2.3.2. 3-scan trace acquisition at  $0.5 \times 0.5 \times 2.0 \text{ mm}^3$  voxel size

127    As listed in Table 1, Protocol #4 was implemented based on NAViEPI  
128    with five shots per diffusion encoding. This protocol was compared against  
129    single-shot EPI (Protocol #3) with the same spatial resolution and acceler-  
130    ation, such as to demonstrate the sampling efficiency of NAViEPI.

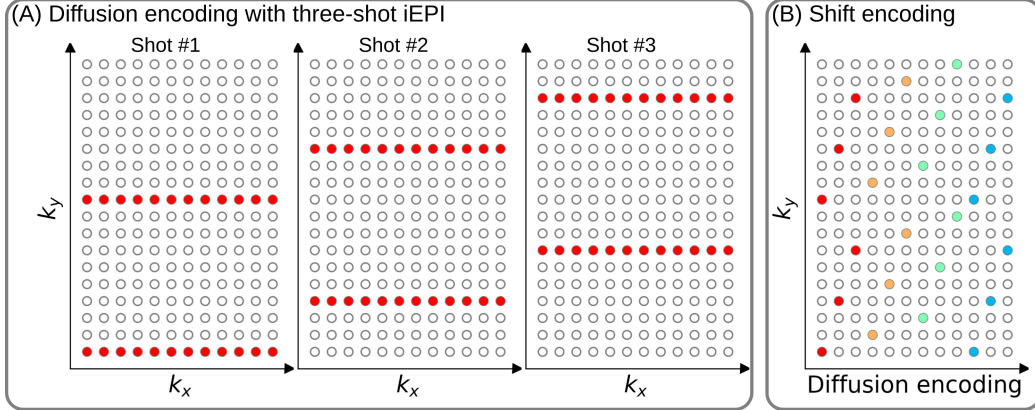


Figure 1: (A) An example DW-MRI acquisition with three-shot interleaved EPI acquisition. (B) The proposed  $k_y$  shifted diffusion encoding scheme. This example employs three shots per DW image. Therefore, every three columns have the same color.

131 *2.4. Forward modeling*

132 Our proposed acquisition method yields multi-dimensional **multi-band** R1.25  
133  $k$ -space data  $\mathbf{y}_{c,q,s}$ , where  $c, q, s$  denotes the index of the coil sensitivity map, the diffusion encoding, and the shot, respectively. **Acquisition modeling** needs to consider several aspects. R1.26

136 First, the acquired  $k$ -space data  $\mathbf{y}$  is mapped from individual shot images 137  $\mathbf{x}_{q,s,z}$  via the forward model,

$$\begin{aligned} \mathbf{y}_{c,q,s} &= \mathbf{P}_{q,s} \Sigma \Theta_z \mathbf{F} \mathbf{S}_c \mathbf{x}_{q,s,z} \\ \mathbf{y} &\coloneqq \mathbf{E}_1 \mathbf{x} \end{aligned} \tag{1}$$

138 Here, the encoding matrix  $\mathbf{E}_1$  comprises a chain of linear operators. Every 139 shot image  $\mathbf{x}$  is point-wise multiplied by a set of coil sensitivity maps ( $\mathbf{S}$ ) and 140 Fourier transformed ( $\mathbf{F}$ ). The output is then point-wise multiplied by the

141 multi-slice phase map ( $\Theta$ ) with  $z$  the slice index in simultaneously excited  
 142 slices. This operator shifts individual slice along the phase-encoding direction  
 143 via varying phase modulation (Breuer et al., 2005). The SMS  $k$ -space data  
 144 is then summed (collapsed,  $\Sigma$ ) along the slice dimension and masked (point-  
 145 wise multiplied,  $\mathbf{P}$ ) by the sampling pattern of each diffusion encoding and  
 146 shot.

R1.27

147 Second, for diffusion MRI based on multi-shot EPI, multiple shots ac-  
 148 quired for a given diffusion encoding need to be combined as one DW image R1.28  
 149 ( $\tilde{\mathbf{x}}$ ). A possibility is to perform magnitude average (Chen et al., 2013) or R1.29  
 150 root-sum-squares (RSS) (Mani et al., 2017) of shot images. This method  
 151 is robust to in-plane motion, but sub-optimal concerning SNR (Guhaniyogi R3.27  
 152 et al., 2016). Alternatively, shot combination can be done via shot-to-shot R1.30  
 153 phase variation correction (Liu et al., 2005; Chen et al., 2013). This can  
 154 be incorporated to our formulation as point-wise multiplication between the R1.31  
 155 shot-to-shot phase variation ( $\Phi$ ) and the DW image ( $\tilde{\mathbf{x}}$ ),

$$\mathbf{x}_{q,s,z} = \Phi_{q,s,z} \tilde{\mathbf{x}}_{q,z} \quad (2)$$

156 Note that  $\tilde{\mathbf{x}}$  can be obtained by applying the adjoint of  $\Phi$  to  $\mathbf{x}$ . In MUSE,  
 157  $\Phi$  is obtained by parallel imaging reconstruction of all shots with subsequent  
 158 phase smoothing of every shot image. Based on this phase correction, the  
 159 complete forward model follows

$$\mathbf{y} := \mathbf{E}_2 \tilde{\mathbf{x}} = \mathbf{E}_1 \Phi \tilde{\mathbf{x}} \quad (3)$$

160 where the encoding matrix  $\mathbf{E}_2$  comprises the chain of the shot-to-shot phase  
 161 variation  $\Phi$  and the encoding matrix  $\mathbf{E}_1$ . We implemented these two encoding  
 162 matrices in SigPy (Ong and Lustig, 2019).

163    2.5. Joint  $k$ - $q$ -slice reconstruction

164    Based on the generalized forward models in Eqs. (1) and (3), our proposed  
165    joint  $k$ - $q$ -slice reconstruction can be formulated as a three-step approach.

166    **I. Navigator echo reconstruction.** The acquisition of navigator echoes  
167    follows the forward model in Eq. (1), so the reconstruction of navigator  
168    echoes can be formulated as:

$$\operatorname{argmin}_{\mathbf{x}} \|\mathbf{y} - \mathbf{E}_1 \mathbf{x}\|_2^2 + \lambda \mathbf{R}(\mathbf{x}) \quad (4)$$

169    where  $\mathbf{R}(\mathbf{x})$  denotes the regularization functional with the regulariza-  
170    tion strength  $\lambda$ . In this work,  $\ell^2$  regularization was used, i.e.,  $\mathbf{R}(\mathbf{x}) =$   
171     $\|\mathbf{x}\|_2^2$ .

172    **II. Iterative phase smoothing.** Shot-to-shot phase variation was ex-  
173    tracted from the reconstructed navigator echo phases. Assuming that R1.13  
174    phase images are spatially smooth (Chen et al., 2013; Dai et al., 2023),  
175    we employed the iterative approach to smooth phase,

$$\mathbf{x}^{(k+1)} = \mathbf{F}^{-1} \mathcal{H} \mathbf{F} \mathbf{x}^{(k)} \quad (5)$$

176    where the index  $k$  denotes the iteration, and  $x^{(0)}$  is then the recon-  
177    structed navigator image from Step I.  $\mathcal{H}$  is the Hanning window.

178    **III. Shot-combined reconstruction.** Joint reconstruction of all DW im-  
179    ages using the shot-combined forward model  $\mathbf{E}_2$  with shot-to-shot phase  
180    variation from Step II reads:

$$\operatorname{argmin}_{\tilde{\mathbf{x}}} \|\mathbf{y} - \mathbf{E}_2 \tilde{\mathbf{x}}\|_2^2 + \lambda \|\mathbf{T} \tilde{\mathbf{x}}\|_* \quad (6)$$

181    Here, LLR regularization was employed in the local spatial-diffusion  
182    matrices, based on the theory of partially separable functions (Liang,

2007; Trzasko and Manduca, 2011; Zhang et al., 2015).  $\mathbf{T}$  represents a linear operator that firstly slides a local patch window through all DW images and then flattens every set of local patches to two-dimensional (2D) matrices, comprising spatial and diffusion dimensions. The nuclear norm regularization is enforced via singular value thresholding (SVT) of all flattened 2D matrices (Cai et al., 2010). We implemented this regularization term as a proximal operator (Beck, 2017).

This work employed blipped-CAIPI SMS (Setsompop et al., 2012), in which spatially separated slices are simultaneously excited and acquired. Therefore, 2D instead of 3D patches were used to construct the spatial-diffusion matrices.

It has been reported that LLR is prone to checkerboard artifacts when  $\lambda$  is too large (Hu et al., 2020). We overcame this problem by utilizing overlapping blocks and providing an efficient implementation. If the blocks overlap,  $\mathbf{T}^H \mathbf{T}$  input  $\neq$  input, where  $\mathbf{T}^H$  denotes the Hermitian adjoint operator of  $\mathbf{T}$ . This is because overlapping values are summed in the output of  $\mathbf{T}^H$ . Our efficient implementation was to scale  $\mathbf{T}^H$  as  $(1/\text{divisor})\mathbf{T}^H$ , where the divisor matrix was obtained by  $\mathbf{T}^H \mathbf{T} \mathbf{1} \cdot \mathbf{1}$  denoted the matrix of all ones with the same shape as the input.

202 2.6. Reconstruction

The acquired raw data was read in by `twixtools` (<https://github.com/pehses/twixtools>). Ramp-sampling regridding and FOV/2-ghost correction were also performed in `twixtools`. Subsequently, coil sensitivity maps were computed from reference scans using `ESPIRiT` (Uecker et al., 2014) in `SigPy` (Ong and Lustig, 2019).

208 With this pre-processing as well as the implemented forward models and R1.39  
 209 proximal operator, the inverse problem in Eq. (6) was solved by the alter-  
 210 nating direction method of multipliers (ADMM) (Boyd et al., 2010).

211 ADMM solves the minimization problems in an alternating update scheme,

$$\begin{cases} \mathbf{x}^{(k+1)} := \underset{\mathbf{x}}{\operatorname{argmin}} \| \mathbf{y} - \mathbf{E}(\mathbf{x}) \|^2 + \rho/2 \| \mathbf{T}\mathbf{x} - \mathbf{z}^{(k)} + \mathbf{u}^{(k)} \|_2^2 \\ \mathbf{z}^{(k+1)} := \mathcal{T}_{\lambda/\rho}(\mathbf{T}\mathbf{x}^{(k+1)} + \mathbf{u}^{(k)}) \\ \mathbf{u}^{(k+1)} := \mathbf{u}^{(k)} + \mathbf{T}\mathbf{x}^{(k+1)} - \mathbf{z}^{(k+1)} \end{cases} \quad (7)$$

212 where  $k$  denotes the ADMM iteration.  $\mathbf{z}$  is the auxiliary variable ( $\mathbf{z} = \mathbf{T}\mathbf{x}$ ),  
 213 and  $\mathbf{u}$  is the Lagrangian multipliers. Importantly, when solving Eq. (1),  $\mathbf{x}$   
 214 denotes shot images and  $\mathbf{E}$  denotes  $\mathbf{E}_1$  in Eq. (7). In contrast,  $\mathbf{x}$  denotes shot-  
 215 combined images and  $\mathbf{E}$  denotes  $\mathbf{E}_2$  when solving Eq. (3).  $\mathbf{x}$  can be solved  
 216 using linear least square algorithms, e.g. conjugate gradients (Hestenes and R3.35  
 217 Stiefel, 1952), while  $\mathbf{z}$  is updated via singular value thresholding ( $\mathcal{T}$ ) with R2.8,  
 218 the thresholding parameter  $\lambda/\rho$ . The coupling parameter  $\rho$  is effective in R3.32  
 219 both the update of  $\mathbf{x}$  and  $\mathbf{z}$ . It acts as Tikhonov regularization strength  
 220 when updating  $\mathbf{x}$ , but also inversely scales the thresholding strength when  
 221 updating  $\mathbf{z}$ , as shown in Supporting Information Figures S1 and S2.

222 In this work, 15 ADMM iterations with  $\rho = 0.05$  and  $\lambda = 0.04$ , and a  
 223 block size of 6 for LLR (refer to Supporting Information Figure S3) were  
 224 used. All reconstructions were done on a single A100 SXM4/NVLink GPU  
 225 with 40 GB memory (NVIDIA, Santa Clara, CA, USA). R3.37

226 We compared our proposed joint reconstruction with established multi-  
 227 shot reconstruction techniques, specifically, MUSE (Chen et al., 2013) and  
 228 JULEP (Dai et al., 2023). Here, MUSE and JULEP are hosted on GitHub R1.3  
 229 by Dr. Dai, and MUSSELS with the multi-band reconstruction feature is

230 made available by Dr. Bilgic. Further, we performed the local-PCA denoising  
231 (Cordero-Grande et al., 2019) as implemented in MRtrix (Tournier et al., 2019)  
232 on the MUSE reconstructed complex DW images.

233 With reconstructed DW images, fractional anisotropy (FA) maps (Basser  
234 et al., 1994) were fitted using our implementation in Python, whereas fiber  
235 orientation distribution functions (fODF) (Aganj et al., 2009) were computed  
236 in MITK-Diffusion (Fritzsche et al., 2012) with the spherical harmonic order  
237 4 and the regularization factor 0.002. fODF maps were displayed with the  
238 min-max normalization and the FA/GFA (generalized fractional anisotropy) R1.41,  
239 scaling factor 2.2. R3.41

240 **3. Results**

241 *3.1. Iterative smoothing of shot-to-shot phase variation*

242 Navigators were acquired with the acceleration rate as listed in Table 1.  
243 Besides, the base resolution of navigators was smaller than imaging echoes.  
244 As a result, reconstructed navigator phases (refer to the first column in Fig. 2)  
245 from Step I in Section 2.5 are not spatially smooth. Such phases, when  
246 used in the shot-combined reconstruction, result in signal void artifacts in  
247 DW images. To address this problem, we utilized the iterative smoothing  
248 procedure. As shown in Fig. 2, the ripple-like phase artifact disappears after  
249 five iterations. It can also be seen that such iterative procedure retains the  
250 shot-to-shot phase variation.

251 *3.2. Comparison to MUSE and JULEP with four-shot iEPI acquisition*

252 The iterative phase smoothing was also applicable to MUSE-type self- R1.1,  
253 navigating reconstruction, where shot phases were reconstructed from imag- R1.2  
254 ing echoes. Fig. 3 compares our proposed JETS with MUSE (Chen et al.,  
255 2013), MUSE with complex-valued local-PCA denoiser (Cordero-Grande et al.,  
256 2019), and JULEP (Dai et al., 2023). The residual noise from MUSE can be  
257 largely removed by the denoiser. However, when compared to JETS, the de-  
258 noiser shows residual noise patterns within the globus pallidus (indicated by  
259 the red arrow). JETS also shows better denoising than JULEP. The reason  
260 is that JETS enforces spatial-diffusion regularization, whereas JULEP for-  
261 mulates structured low-rank regularization of the four shots for one diffusion  
262 encoding.

### Iterative smoothing of shot-to-shot phase variation

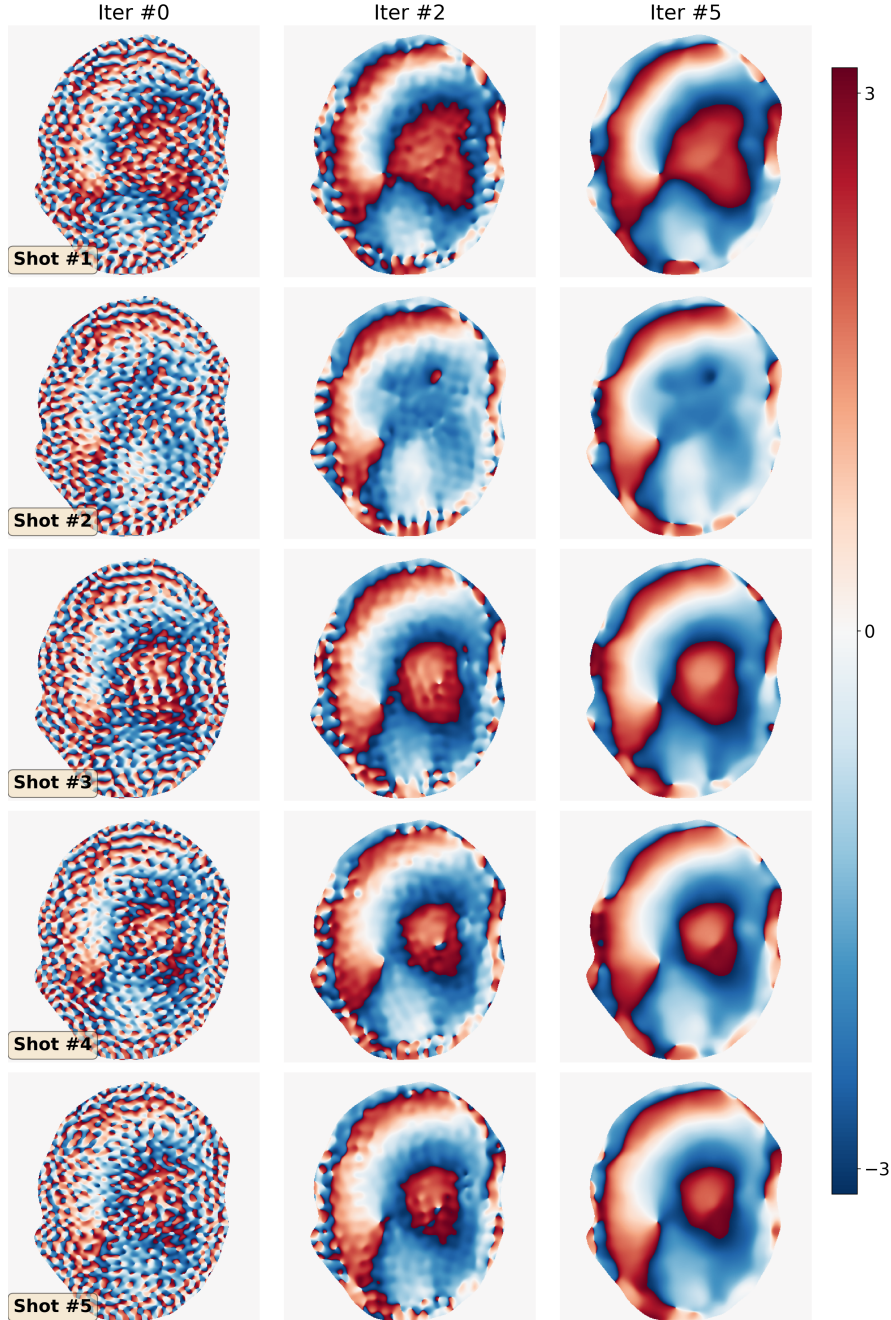


Figure 2: Iterative smoothing of shot-to-shot phase variation according to Eq. (5). Navigators from Protocol #3 were reconstructed based on Step I in Section 2.5 and then used as the input (iter #0, left column).

**8th DW image from 4-shot iEPI @ 1 mm ISO**

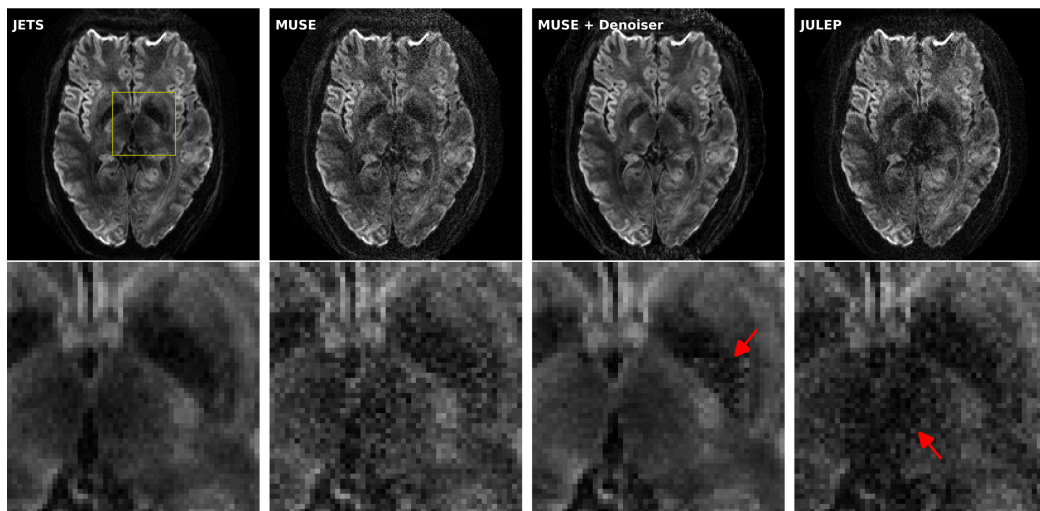


Figure 3: Reconstructed DW images (the 8th diffusion encoding) based on 4-shot iEPI acquisition with 1 mm isotropic resolution (Protocol #1 in Table 1). Four reconstruction methods are compared (from left to right): JETS, MUSE, MUSE with denoiser, and JULEP. The 2nd row displays the magnified views of the yellow square.

263    *3.3. Retrospectively undersampling from the four-shot iEPI acquisition*

264    JETS reconstruction results on the four-shot prospectively fully-sampled R1.1  
265    data from Protocol #1 in Table 1, as well as on the retrospectively under-  
266    sampled one-shot data without and with the proposed  $k_y$  shift are displayed  
267    in Fig. 4. Residual aliasing artifacts are visible in the reconstruction without  
268     $k_y$  shifting, as pointed by the red arrows. On the contrary, the reconstruction  
269    with the proposed  $k_y$  shifting among diffusion encodings shows much reduced  
270    aliasing, reduced noise, and higher SSIM.

271    *3.4. Analysis of reconstruction parameters*

272    Here we provide a systematic analysis of the proposed JETS reconstruc- R1.4  
273    tion with LLR regularization applied to the spatial-diffusion dimension.

274    First, we varied the regularization strength  $\lambda$  from 0, to 0.08, and to  
275    0.16. The reconstruction with  $\lambda = 0$  in Eq. (6) corresponds to parallel  
276    imaging reconstruction without LLR regularization. It is worth noting that  
277    the proposed NAViEPI sequence demonstrates high-quality sub-millimeter  
278    DW images ( $0.5 \times 0.5 \times 2.0 \text{ mm}^3$  in this example). The DW images can be  
279    further improved with the use of LLR regularization, i.e., reduced noise, as  
280    seen in the reconstruction with  $\lambda = 0.08$ . Increasing  $\lambda$  (e.g. 0.16) further  
281    reduces noise, but at the cost of increased blurring. Therefore,  $\lambda = 0.08$  was  
282    selected in this work.

283    Second, besides the regularization strength, the block size (i.e., the width  
284    of square 2D patches) also plays a role in denoising. Here, the block size of 3  
285    shows the best denoising as compared to 6 and 9, especially in the peripheral  
286    brain region. According to (Cordero-Grande et al., 2019), it is suggested  
287    to keep the patch size roughly equal to the diffusion encoding length. In

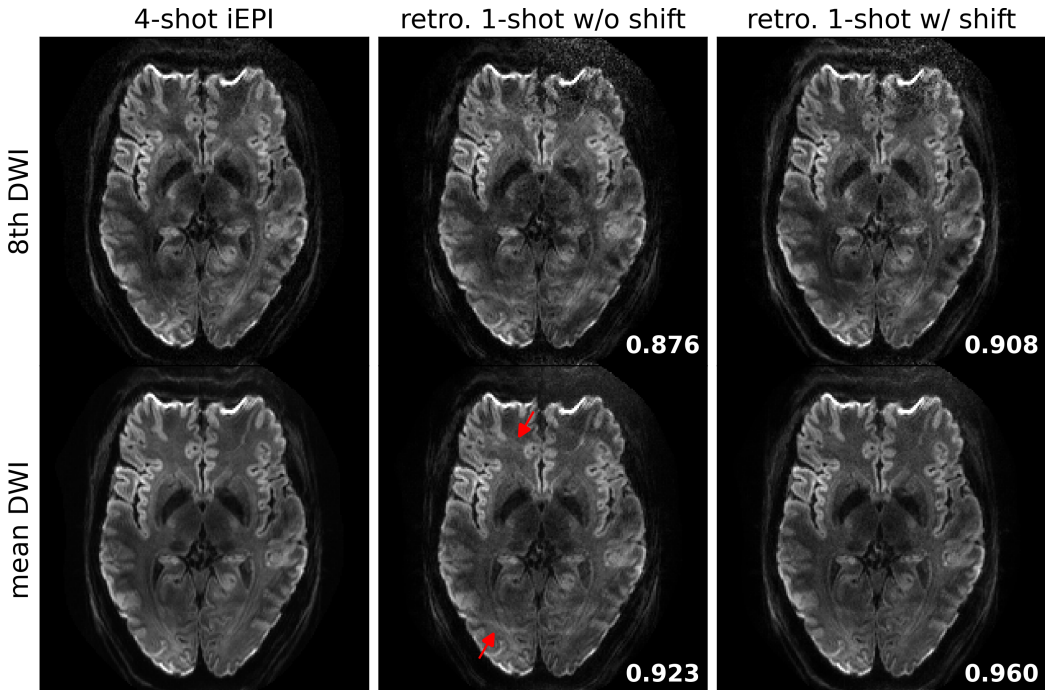


Figure 4: Quantitative validation of the proposed  $k_y$ -shift encoding sampling pattern based on 4-shot iEPI acquisition with 1 mm isotropic resolution (Protocol #1 in Table 1). (Top) the 8th diffusion encoding and (bottom) mean DWI over 20 diffusion encodings. (1st column) JETS reconstruction of 4-shot iEPI acquisition is used as the ground truth. The 2nd and the 3rd column displays JETS reconstruction of retrospectively undersampled 1-shot acquisition without and with  $k_y$  shifting, respectively. structural similarity (SSIM) values are computed and displayed in the bottom right corners.

288 this 3-scan trace acquisition example, the diffusion encoding length is 4 (1  $b_0$   
289 plus 3 orthogonal diffusion directions). Among the tested block sizes, 3 is the  
290 closest to 4, and hence renders better denoising, whereas the other block sizes  
291 may require stronger regularization strength. In practice, we also observed  
292 that smaller block sizes construct smaller matrices for SVT and thus lead to  
293 shorter computation time.

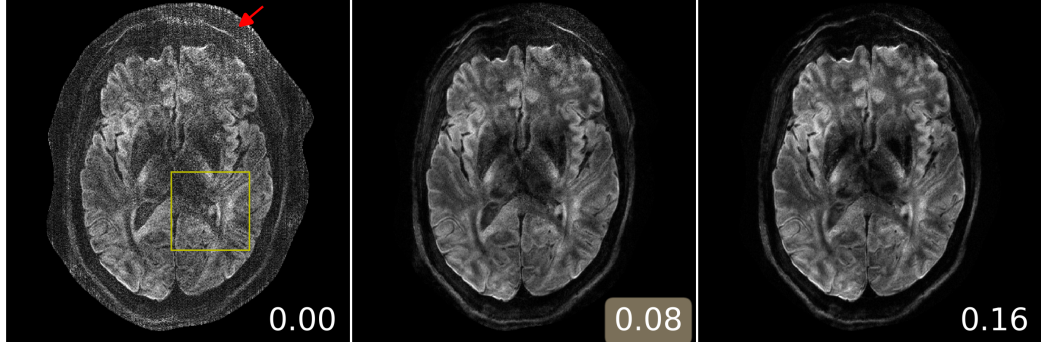
294 Third, we varied the stride, i.e., the increment from one local patch to  
295 the next. When the block size equals the stride (6 in this example), it refers  
296 to non-overlapping LLR, which is prone to checkerboard artifacts even with  
297 the use of random shifting ([Saucedo et al., 2017](#)) in each ADMM iteration,  
298 as indicated by the red arrows in the magnified views of Fig. 5. Therefore,  
299 we utilized the overlapping LLR with the stride of 1, which requires the  
300 implementation of the scaling matrix in Section 2.5 to avoid the summation  
301 of overlapped pixels. The drawback of overlapping LLR, however, is the  
302 increased number of matrices for SVT and hence the increased computation  
303 time ([Saucedo et al., 2017](#)).

304 *3.5. Sampling efficiency of NAViEPI*

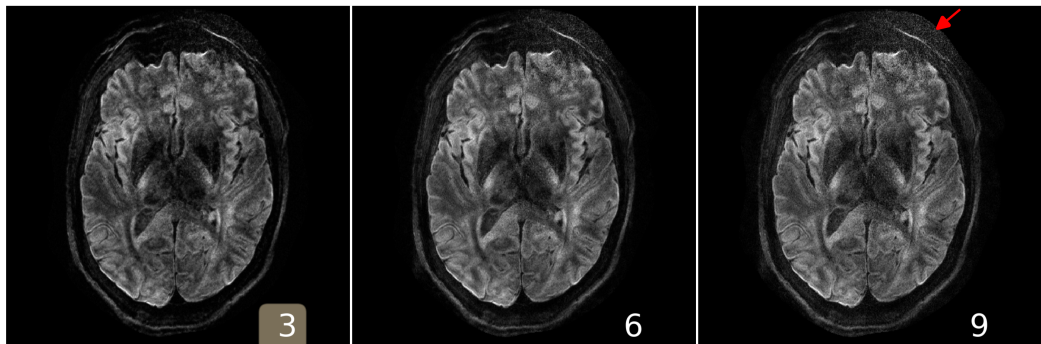
305 As shown in Fig. 6, NAViEPI achieves sub-millimeter resolution (voxel R3.5  
306 size  $0.5 \times 0.5 \times 2.0 \text{ mm}^3$ ) with the use of 5-shot acquisition. When compared  
307 to the single-shot acquisition with the same voxel size, the acquisition time  
308 of NAViEPI is about two times longer, but the image quality of NAViEPI is  
309 remarkably improved.

310 In the sub-millimeter imaging scenario, the increased base resolution re-  
311 quires longer TE (143 ms) in the single-shot acquisition, which results in  
312 significant signal loss due to  $T_2$  relaxation. Therefore, sub-millimeter DWI

**(A) varying  $\lambda$ , keeping block as 6 and stride as 1**



**(B) varying block size, keeping  $\lambda$  as 0.08 and stride as 1**



**(C) varying stride, keeping  $\lambda$  as 0.08 and block as 6**

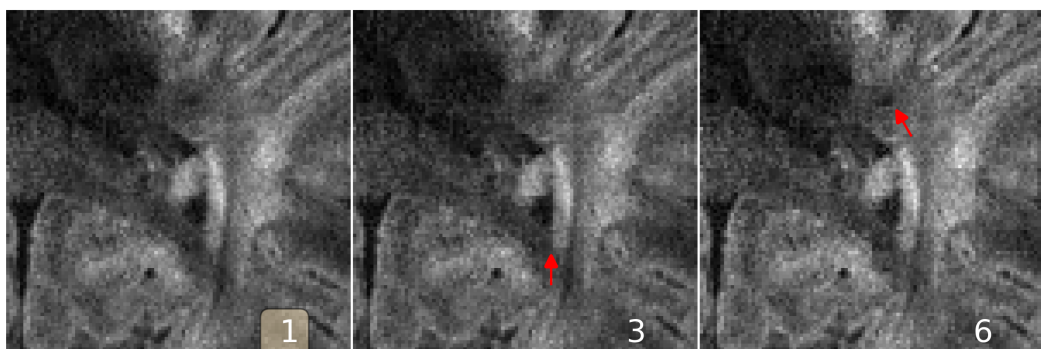


Figure 5: Analysis of reconstruction parameters based on the 3-scan trace acquisition with  $0.5 \times 0.5 \times 2.0 \text{ mm}^3$  (Protocol #3 in Table 1). Displayed are JETS reconstructed single-direction DW images. **(A)** Varying the regularization strength  $\lambda$  from 0 to 0.08 and 0.16. **(B)** Varying the block size from 3 to 6 and 9. **(C)** Varying the stride size from 1 to 3 and 6 (non-overlapping).

313 necessitates multi-shot acquisition, which is subject to shot-to-shot phase  
314 variation and long scan time. However, NAViEPI solves both challenges. The  
315 5-shot acquisition reduces TE to 58 ms, and thus retains SNR significantly  
316 compared to the single-shot acquisition. Moreover, the JETS reconstruction  
317 can help to reduce noise and improve structural visibility.

318 Fig. 7 shows the JETS reconstructed  $b_0$  and TRACE images in different R1.7  
319 slice locations. Admittedly, the lower brain region (e.g. slice #22) exhibits in-  
320 homogeneous and lower signal intensity than the upper slices. Such inhomomo-  
321 geneity can be alleviated with the use of multi-channel parallel transmission  
322 (Katscher et al., 2003; Grissom et al., 2010).

**3-scan trace acquisition with voxel size  $0.5 \times 0.5 \times 2.0 \text{ mm}^3$**

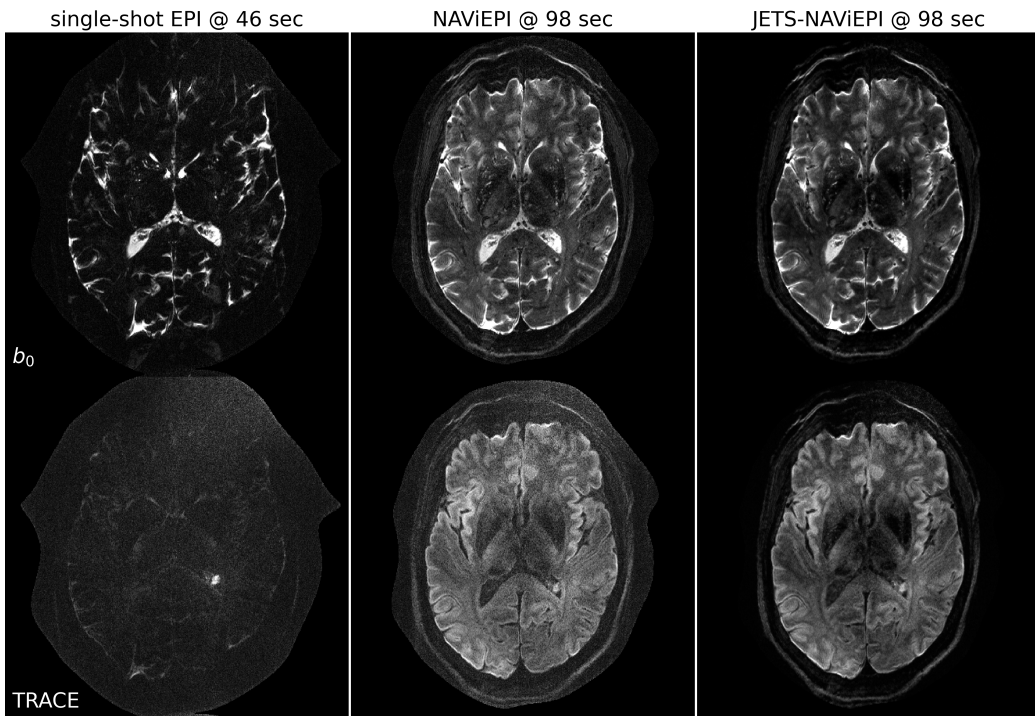


Figure 6: Sampling efficiency of the proposed NAViEPI sequence. 5-shot NAViEPI acquisition with the voxel size  $0.5 \times 0.5 \times 2.0 \text{ mm}^3$  (Protocol #3) was compared with single-shot EPI acquisition (Protocol #4). Both the 1st and the 2nd columns were reconstructed via parallel imaging without LLR regularization, whereas the 3rd column was reconstructed via JETS.

**3-scan trace acquisition with voxel size  $0.5 \times 0.5 \times 2.0 \text{ mm}^3$**

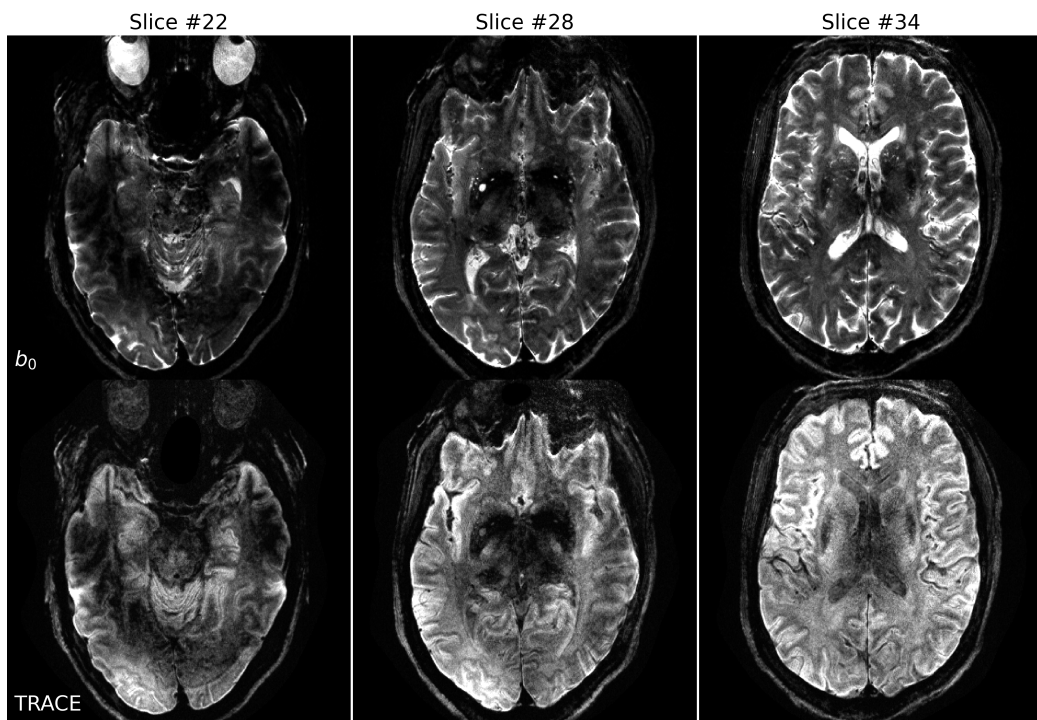


Figure 7: Reconstruction of the 3-scan trace acquisition with the voxel size  $0.5 \times 0.5 \times 2.0 \text{ mm}^3$  (Protocol #3) at different slices.

323 **4. Discussion**

324 This work reports a novel DW-MRI technique, JETS-NAViEPI. NAViEPI  
325 (1) achieves the fast and efficient acquisition of both imaging and navigator  
326 echoes, (2) enforces consistent bandwidth between the echoes, and (3) al-  
327 lows for undersampled iEPI as well as a large number of shots. Moreover,  
328 compared to the single-shot acquisition, joint  $k$ - $q$ -space reconstruction with  
329  $k_y$ -shift encoding on NAViEPI retains SNR and reduces aliasing artifacts in  
330 DW images. As a result, JETS-NAViEPI renders high spatiotemporal reso-  
331 lution diffusion MRI protocols in 7 T, e.g., 3-scan trace acquisition with the  
332 voxel size  $0.5 \times 0.5 \times 2.0 \text{ mm}^3$  at 1.5 min.

333 One limitation of JETS-NAViEPI is the long reconstruction time due to R3.48  
334 the simultaneous reconstruction of all DW images and the use of overlapping  
335 locally low-rank regularization. The reconstruction for the Protocol #3 in  
336 Table 1 on an A100 GPU takes about 2 min per multi-band slice. To reduce R3.48  
337 the computation time, coil compression algorithms (Buehrer et al., 2007;  
338 Huang et al., 2008) can be employed to reduce the number of coils for image  
339 reconstruction. Moreover, one may deploy multi-GPU distributed computing  
340 or modern optimization algorithms (e.g. stochastic gradient descent) (Ong  
341 et al., 2020) to speed up the reconstruction.

342 Neither the signal modeling in Eqs. (1) and (3) nor the LLR regulariza- R1.5  
343 tion considers the subject motion. In the presence of motion, the regularized  
344 reconstruction may degrade. To overcome this problem, scout-informed mo-  
345 tion estimation and reconstruction (Polak et al., 2022) could be integrated  
346 into the framework.

347 Another potential extension of this work is to incorporate distortion cor-

348 rection. The standard distortion correction method is known as TOPUP  
349 (Andersson et al., 2003), which acquires two scans with opposing phase-en-  
350 coding directions to obtain the field inhomogeneity map and then performs  
351 conjugate phase reconstruction to correct for distortion.

352 This work employed a single regularization weight  $\lambda$  to enforce low rank-  
353 ness along the spatial-diffusion direction. However, SNR may be heteroge-  
354 neous within the FOV. Therefore, one single regularization scalar may be  
355 inadequate to cover the whole FOV. Beyond this SVT-based machine-learn-  
356 ing reconstruction, one may seek to learn a  $q$ -space prior as the regularizer  
357 (Hammernik et al., 2018; Mani et al., 2021).

358 Although NAViEPI employs navigators for the acquisition of shot-to- R1.13  
359 shot phase variation, it is worth noting that phase behavior depends on  
360 several hard-to-control factors such as pulsatile motion, bulk motion, loca-  
361 tions within the brain, and diffusion sensitization strength. Therefore, more  
362 comprehensive modeling or post-processing such as image registration may  
363 be considered in future work.

364 While this work reconstructs all DW images and then performs model  
365 fitting, an alternative approach is to directly estimate  $b_0$  and diffusion tensors  
366 from measured  $k$ - $q$ -space data using model-based reconstruction (Knoll et al.,  
367 2015; Dong et al., 2018; Shafieizargar et al., 2023). Compared to DW image  
368 reconstruction, model-based reconstruction solves for a fewer number of un- R3.49  
369 knowns, but requires strict diffusion tensor modeling and the use of nonlinear  
370 least square solvers.

371 **5. Conclusions**

372 We demonstrated the JETS-NAViEPI technique, which integrates a  $k_y$ -  
373 shifted encoding interleaved EPI sequence and a joint reconstruction with  
374 overlapping locally low-rank regularization for high spatial-angular-temporal  
375 resolution DW-MRI at 7 T. This technique allows for high-quality DW image  
376 reconstruction with accelerated acquisitions.

377 **Funding**

378 This work was supported by Deutsche Forschungsgemeinschaft (DFG) –  
379 Project Number 513220538, as well as National Institutes of Health (NIH)  
380 R01 EB024532 and P41 EB017183.

381 **Data and code available statement**

382 In the spirit of reproducible and open science, we will publish our source  
383 code (<https://github.com/ZhengguoTan/sigpy>) as well as the raw  $k$ -space  
384 data (<https://doi.org/10.5281/zenodo.7548595>) during the review pro-  
385 cess.

386 **Acknowledgments**

387 The authors thank Dr. Peter Neher for the discussion on MITK-Diffusion.  
388 The authors gratefully acknowledge the scientific support and HPC resources  
389 provided by the Erlangen National High Performance Computing Center  
390 (NHR@FAU) of Friedrich-Alexander-Universität Erlangen-Nürnberg (FAU)  
391 under the NHR project b143dc. NHR funding is provided by federal and

392 Bavarian state authorities. NHR@FAU hardware is partially funded by the  
393 German Research Foundation (DFG) – 440719683.  
394 The authors thank Dr. Berkin Bilgic for making the MUSSELS source R1.2  
395 code (<https://bit.ly/2QgBg9U>) publically available, Dr. Erpeng Dai for  
396 sharing the JULEP source code (<https://github.com/daiep/JULEP>) on  
397 GitHub, and Dr. Zhiyong Zhang for sharing the SPA-LLR source code (<https://github.com/ZZgroupSJTU/PMCmsDTI>) on GitHub. The authors also thank  
398 Dr. Philipp Ehses for the discussion on the use of twixtools (<https://github.com/pehses/twixtools>).  
399  
400

401 **References**

- 402 Aganj, I., Lenglet, C., Sapiro, G., 2009. Odf reconstruction in q-ball imag-  
403 ing with solid angle consideration, in: Proc. IEEE Int. Symp. Biomed.  
404 Imaging, pp. 1398–1401. doi:[10.1109/ISBI.2009.5193327](https://doi.org/10.1109/ISBI.2009.5193327).
- 405 Andersson, J.L.R., Skare, S., Ashburner, J., 2003. How to correct suscepti-  
406 bility distortions in spin-echo echo-planar images: application to diffusion  
407 tensor imaging. NeuroImage 20, 870–888. doi:[10.1016/S1053-8119\(03\)00336-7](https://doi.org/10.1016/S1053-8119(03)00336-7).
- 408  
409 Bammer, R., Keeling, S.L., Augustin, M., Pruessmann, K.P., Wolf, R., Stoll-  
410 berger, R., Hartung, H.P., Fazekas, F., 2001. Improved diffusion-weighted  
411 single-shot echo-planar imaging (EPI) in stroke using sensitivity encoding  
412 (SENSE). Magn. Reson. Med. 46, 548–554. doi:[10.1002/mrm.1226](https://doi.org/10.1002/mrm.1226).
- 413 Basser, P.J., Mattiello, J., Le Bihan, D., 1994. MR diffusion tensor

- 414      spectroscopy and imaging. Biophys. J. 66, 259–267. doi:[10.1016/S0006-3495\(94\)80775-1](https://doi.org/10.1016/S0006-3495(94)80775-1).
- 415
- 416      Beck, A., 2017. First-order methods in optimization. Society for In-  
417      dustrial and Applied Mathematics, Philadelphia, PA. doi:[10.1137/1.9781611974997](https://doi.org/10.1137/1.9781611974997).
- 417
- 418
- 419      Bilgic, B., Chatnuntawech, I., Manhard, M.K., Tian, Q., Liao, C., Iyer, S.S.,  
420      Cauley, S.F., Huang, S.Y., Polimeni, J.R., Wald, L.L., Setsompop, K.,  
421      2019. Highly accelerated multishot echo planar imaging through synergistic  
422      machine learning and joint reconstruction. Magn. Reson. Med. 82, 1343–  
423      1358. doi:[10.1002/mrm.27813](https://doi.org/10.1002/mrm.27813).
- 424
- 425      Block, K.T., Uecker, M., Frahm, J., 2007. Undersampled radial MRI with  
426      multiple coils. Iterative image reconstruction using a total variation con-  
427      straint. Magn. Reson. Med. 57, 1186–1098. doi:[10.1002/mrm.21236](https://doi.org/10.1002/mrm.21236).
- 428
- 429
- 430      Boyd, S., Parikh, N., Chu, E., Peleato, B., Eckstein, J., 2010. Distributed  
431      optimization and statistical learning via the alternating direction method  
432      of multipliers. Foundations and Trends in Machine Learning 3, 1–122.  
433      doi:[10.1561/2200000016](https://doi.org/10.1561/2200000016).
- 434
- 435      Breuer, F.A., Blaimer, M., Heidemann, R.M., Mueller, M.F., Griswold, M.A.,  
436      Jakob, P.M., 2005. Controlled Aliasing in Parallel Imaging Results in  
437      Higher Acceleration (CAPIRINHA) for Multi-Slice Imaging. Magn. Re-  
438      son. Med. 53, 684–691. doi:[10.1002/mrm.20401](https://doi.org/10.1002/mrm.20401).
- 439
- 440      Buehrer, M., Pruessmann, K.P., Boesiger, P., Kozerke, S., 2007. Array com-

- 436 pression for MRI with large coil arrays. Magn. Reson. Med 57, 1131–1139.  
437 doi:[10.1002/mrm.21237](https://doi.org/10.1002/mrm.21237).
- 438 Butts, K., Riederer, S.J., Ehman, R.L., Thompson, R.M., Jack, C.R., 1993.  
439 Interleaved echo planar imaging on a standard MRI system. Magn. Reson.  
440 Med. 31, 67–72. doi:[10.1002/mrm.1910310111](https://doi.org/10.1002/mrm.1910310111).
- 441 Cai, J.F., Candès, E.J., Shen, Z., 2010. A singular value threshold-  
442 ing algorithm for matrix completion. SIAM. J. Optim. 20, 1956–1982.  
443 doi:[10.1137/080738970](https://doi.org/10.1137/080738970).
- 444 Chen, N.K., Guidon, A., Chang, H.C., Song, A.W., 2013. A robust multi-  
445 shot scan strategy for high-resolution diffusion weighted MRI enabled by  
446 multiplexed sensitivity-encoding (MUSE). NeuroImage 72, 41–47. doi:[10.1016/j.neuroimage.2013.01.038](https://doi.org/10.1016/j.neuroimage.2013.01.038).
- 448 Cordero-Grande, L., Christiaens, D., Hutter, J., Price, A.N., Hajnal, J.V.,  
449 2019. Complex diffusion-weighted image estimation via matrix recovery  
450 under general noise models. NeuroImage 200, 391–404. doi:[10.1016/j.neuroimage.2019.06.039](https://doi.org/10.1016/j.neuroimage.2019.06.039).
- 452 Dai, E., Ma, X., Zhang, Z., Yuan, C., Guo, H., 2017. Simultaneous multislice  
453 accelerated interleaved EPI DWI using generalized blipped-CAIPI acqui-  
454 sition and 3D K-space reconstruction. Magn. Reson. Med. 77, 1593–1605.  
455 doi:[10.1002/mrm.26249](https://doi.org/10.1002/mrm.26249).
- 456 Dai, E., Mani, M., McNab, J.A., 2023. Multi-band multi-shot diffu-  
457 sion MRI reconstruction with joint usage of structured low-rank con-

- 458 straints and explicit phase mapping. Magn. Reson. Med. 89, 95–111.  
459 doi:[10.1002/mrm.29422](https://doi.org/10.1002/mrm.29422).
- 460 Dai, E., Zhang, Z., Ma, X., Dong, Z., Li, X., Xiong, Y., Yuan, C., Guo, H.,  
461 2018. The effects of navigator distortion and noise level on interleaved EPI  
462 DWI reconstruction: a comparison between image- and *k*-space method.  
463 Magn. Reson. Med. 80, 2024–2032. doi:[10.1002/mrm.27190](https://doi.org/10.1002/mrm.27190).
- 464 Dong, Z., Dai, E., Wang, F., Zhang, Z., Ma, X., Yuan, C., Guo, H., 2018.  
465 Model-based reconstruction for simultaneous multislice and parallel imag-  
466 ing accelerated multishot diffusion tensor imaging. Med. Phys. 45, 3196–  
467 3204. doi:[10.1002/mp.12974](https://doi.org/10.1002/mp.12974).
- 468 Fritzsche, K.H., Neher, P.F., Reicht, I., van Bruggen, T., Goch, C., Reisert,  
469 M., Nolden, M., Zelzer, S., Meinzer, H.P., Stieltjes, B., 2012. MITK diffu-  
470 sion imaging. Methods Inf. Med. 51, 441–448. doi:[10.3414/ME11-02-0031](https://doi.org/10.3414/ME11-02-0031).
- 471 Grissom, W.A., Sacolick, L., Vogel, M.W., 2010. Improving high-field MRI  
472 using parallel excitation. Imaging Med. 2, 675–693. doi:[10.2217/IIM.10.62](https://doi.org/10.2217/IIM.10.62).
- 473
- 474 Griswold, M.A., Jakob, P.M., Heidemann, R.M., Nittka, M., Jellus, V.,  
475 Wang, J., Kiefer, B., Haase, A., 2002. Generalized autocalibrating par-  
476 tially parallel acquisitions (GRAPPA). Magn. Reson. Med. 47, 1202–1210.  
477 doi:[10.1002/mrm.10171](https://doi.org/10.1002/mrm.10171).
- 478 Guhaniyogi, S., Chu, M.L., Chang, H.C., Song, A.W., Chen, N.K., 2016. Mo-  
479 tion immune diffusion imaging using augmented MUSE for high-resolution  
480 multi-shot EPI. Magn. Reson. Med. 75, 639–652. doi:[10.1002/mrm.25624](https://doi.org/10.1002/mrm.25624).

- 481 Hammernik, K., Klatzer, T., Kobler, E., Recht, M.P., Sodickson, D.K., Pock,  
482 T., Knoll, F., 2018. Learning a variational network for reconstruction of  
483 accelerated MRI data. *Magn. Reson. Med.* 79, 3055–3071. doi:[10.1002/mrm.26977](https://doi.org/10.1002/mrm.26977).
- 485 Heidemann, R.M., Porter, D.A., Anwander, A., Feiweier, T., Heberlein, K.,  
486 Knösche, T.R., Turner, R., 2010. Diffusion imaging in humans at 7 T  
487 using readout-segmented EPI and GRAPPA. *Magn. Reson. Med.* 64, 9–  
488 14. doi:[10.1002/mrm.22480](https://doi.org/10.1002/mrm.22480).
- 489 Hestenes, M.R., Stiefel, E., 1952. Methods of conjugate gradients for solving  
490 linear systems. *J. Res. Natl. Bur. Stand.* 49, 409–436. doi:[10.6028/jres.049.044](https://doi.org/10.6028/jres.049.044).
- 492 Hu, Y., Wang, X., Tian, Q., Yang, G., Daniel, B., McNab, J., Hargreaves, B.,  
493 2020. Multi-shot diffusion-weighted MRI reconstruction with magnitude-  
494 based spatial-angular locally low-rank regularization (SPA-LLR). *Magn.*  
495 *Reson. Med.* 83, 1596–1607. doi:[10.1002/mrm.28025](https://doi.org/10.1002/mrm.28025).
- 496 Huang, F., Vijayakumar, S., Li, Y., Hertel, S., Duensing, G.R., 2008. A soft-  
497 ware channel compression technique for faster reconstruction with many  
498 channels. *Magn. Reson. Imaging* 26, 133–141. doi:[10.1016/j.mri.2007.04.010](https://doi.org/10.1016/j.mri.2007.04.010).
- 500 Jeong, H.K., Gore, J.C., Anderson, A.W., 2013. High-resolution human  
501 diffusion tensor imaging using 2-D navigated multishot SENSE EPI at 7  
502 T. *Magn. Reson. Med.* 69, 793–802. doi:[10.1002/mrm.24320](https://doi.org/10.1002/mrm.24320).

- 503 Jones, D.K., 2010. Diffusion MRI: Theory, methods, and applications. Oxford  
504 University Press. doi:[10.1093/med/9780195369779.001.0001](https://doi.org/10.1093/med/9780195369779.001.0001).
- 505 Katscher, U., Börnert, P., Leussler, C., van den Brink, J.S., 2003. Transmit  
506 SENSE. Magn. Reson. Med. 49, 144–150. doi:[10.1002/mrm.10353](https://doi.org/10.1002/mrm.10353).
- 507 Knoll, F., Raya, J.G., Halloran, R.O., Baete, S., Sigmund, E., Bammer, R.,  
508 Block, T., Otazo, R., Sodickson, D.K., 2015. A model-based reconstruction  
509 for undersampled radial spin-echo DTI with variational penalties on the  
510 diffusion tensor. NMR Biomed 28, 353–366. doi:[10.1002/nbm.3258](https://doi.org/10.1002/nbm.3258).
- 511 Le Bihan, D., Breton, E., Lallemand, D., Grenier, P., Cabanis, E., Laval-  
512 Jeantet, M., 1986. MR imaging of intravoxel incoherent motions: appli-  
513 cation to diffusion and perfusion in neurologic disorders. Radiology 161,  
514 401–407. doi:[10.1148/radiology.161.2.3763909](https://doi.org/10.1148/radiology.161.2.3763909).
- 515 Liang, Z.P., 2007. Spatiotemporal imaging with partially separable functions,  
516 in: 2007 4th IEEE International Symposium on Biomedical Imaging: From  
517 Nano to Macro, pp. 988–991. doi:[10.1109/ISBI.2007.357020](https://doi.org/10.1109/ISBI.2007.357020).
- 518 Liu, C., Moseley, M.E., Bammer, R., 2005. Simultaneous phase cor-  
519 rection and SENSE reconstruction for navigated multi-shot DWI with  
520 non-Cartesian  $k$ -space sampling. Magn. Reson. Med. 54, 1412–1422.  
521 doi:[10.1002/mrm.20706](https://doi.org/10.1002/mrm.20706).
- 522 Lustig, M., Donoho, D., Pauly, J.M., 2007. Sparse MRI: The application of  
523 compressed sensing for rapid MR imaging. Magn. Reson. Med. 58, 1182–  
524 1195. doi:[10.1002/mrm.21391](https://doi.org/10.1002/mrm.21391).

- 525 Mani, M., Jacob, M., Kelley, D., Magnotta, V., 2017. Multi-shot sensitivity-  
526 encoded diffusion data recovery using structured low-rank matrix comple-  
527 tion (MUSSELS). *Magn. Reson. Med.* 78, 494–507. doi:[10.1002/mrm.26382](https://doi.org/10.1002/mrm.26382).
- 529 Mani, M., Magnotta, V.A., Jacob, M., 2021. qModeL: A plug-and-play  
530 model-based reconstruction for highly accelerated multi-shot diffusion MRI  
531 using learned priors. *Magn. Reson. Med.* 86, 835–851. doi:[10.1002/mrm.28756](https://doi.org/10.1002/mrm.28756).
- 533 Mansfield, P., 1977. Multi-planar image formation using NMR spin echoes.  
534 *J Phys C* 10, 55–58. doi:[10.1088/0022-3719/10/3/004](https://doi.org/10.1088/0022-3719/10/3/004).
- 535 Maudsley, A.A., 1980. Multiple-line-scanning spin density imaging. *J. Magn.*  
536 *Reson.* 41, 112–126. doi:[10.1016/0022-2364\(80\)90207-3](https://doi.org/10.1016/0022-2364(80)90207-3).
- 537 Merboldt, K.D., Hanicke, W., Frahm, J., 1985. Self-diffusion NMR imag-  
538 ing using stimulated echoes. *J. Magn. Reson.* 64, 479–486. doi:[10.1016/0022-2364\(85\)90111-8](https://doi.org/10.1016/0022-2364(85)90111-8).
- 540 Mori, S., Crain, B.J., Chacko, V.P., Van Zijl, P.C.M., 1999. Three-  
541 dimensional tracking of axonal projections in the brain by mag-  
542 netic resonance imaging. *Ann. Neurol.* 45, 265–269. doi:[10.1002/1531-8249\(199902\)45:2<265::AID-ANA21>3.0.CO;2-3](https://doi.org/10.1002/1531-8249(199902)45:2<265::AID-ANA21>3.0.CO;2-3).
- 544 Ong, F., Lustig, M., 2019. SigPy: A Python package for high performance  
545 iterative reconstruction, in: Proceedings of the 27th Annual Meeting of  
546 ISMRM, Montréal, CAN, p. 4819. doi:[10.5281/zenodo.5893788](https://doi.org/10.5281/zenodo.5893788).

- 547 Ong, F., Zhu, X., Cheng, J.Y., Johnson, K.M., Larson, P.E.Z., Vasanawala,  
548 S.S., Lustig, M., 2020. Extreme MRI: Large-scale volumetric dynamic  
549 imaging from continuous non-gated acquisitions. Magn. Reson. Med. 84,  
550 1763–1780. doi:[10.1002/mrm.28235](https://doi.org/10.1002/mrm.28235).
- 551 Pipe, J.G., Farthing, V.G., Forbes, K.P., 2002. Multishot diffusion-weighted  
552 FSE using PROPELLER MRI. Magn. Reson. Med. 47, 42–52. doi:[10.1002/mrm.10014](https://doi.org/10.1002/mrm.10014).
- 554 Polak, D., Splitthoff, D.N., Clifford, B., Lo, W.C., Huang, S.Y., Conklin, J.,  
555 Wald, L.L., Setsompop, K., Cauley, S., 2022. Scout accelerated motion  
556 estimation and reduction (SAMER). Magn. Reson. Med. 87, 163–178.  
557 doi:[10.1002/mrm.28971](https://doi.org/10.1002/mrm.28971).
- 558 Porter, D.A., Heidemann, R.M., 2009. High resolution diffusion-weighted  
559 imaging using readout-segmented echo-planar imaging, parallel imaging  
560 and a two-dimensional navigator-based reacquisition. Magn. Reson. Med.  
561 62, 468–475. doi:[10.1002/mrm.22024](https://doi.org/10.1002/mrm.22024).
- 562 Pruessmann, K.P., Weiger, M., Scheidegger, M.B., Boesiger, P., 1999.  
563 SENSE: Sensitivity encoding for fast MRI. Magn. Reson. Med. 42, 952–  
564 962. doi:[10.1002/\(SICI\)1522-2594\(199911\)42:5<952::AID-MRM16>3.0.CO;2-S](https://doi.org/10.1002/(SICI)1522-2594(199911)42:5<952::AID-MRM16>3.0.CO;2-S).
- 566 Ra, J.B., Rim, C.Y., 1993. Fast imaging using subencoding data sets from  
567 multiple detectors. Magn. Reson. Med. 30, 142–145. doi:[10.1002/mrm.1910300123](https://doi.org/10.1002/mrm.1910300123).

- 569 Roemer, P.B., Edelstein, W.A., Hayes, C.E., Souza, S.P., Mueller, O.M.,  
570 1990. The NMR phased array. Magn. Reson. Med. 16, 192–225. doi:[10.1002/mrm.1910160203](#).
- 571
- 572 Saucedo, A., Lefkimiatis, S., Rangwala, N., Sung, K., 2017. Improved com-  
573 putational efficiency of locally low rank MRI reconstruction using iterative  
574 random patch adjustments. IEEE Trans. Med. Imaging 36, 1209–1220.  
575 doi:[10.1109/TMI.2017.2659742](#).
- 576 Setsompop, K., Fan, Q., Stockmann, J., Bilgic, B., Huang, S., Cauley, S.F.,  
577 Nummenmaa, A., Wang, F., Rathi, Y., Witzel, T., Wald, L.L., 2018. High-  
578 resolution *in vivo* diffusion imaging of the human brain with generalized  
579 slice dithered enhanced resolution: Simultaneous multislice (gSlider-SMS).  
580 Magn. Reson. Med. 79, 141–151. doi:[10.1002/mrm.26653](#).
- 581 Setsompop, K., Gagoski, B.A., Polimeni, J.R., Witzel, T., Wedeen, V.J.,  
582 Wald, L.L., Adalsteinsson, E., 2012. Blipped-controlled aliasing in parallel  
583 imaging for simultaneous multislice echo planar imaging with reduced  $g$ -  
584 factor penalty. Magn. Reson. Med. 67, 1210–1224. doi:[10.1002/mrm.23097](#).
- 585
- 586 Shafieizargar, B., Jeurissen, B., Poot, D.H.J., Klein, S., Van Audekerke,  
587 J., Verhoye, M., den Dekker, A.J., Sijbers, J., 2023. ADEPT: Accurate  
588 diffusion echo-planar imaging with multi-contrast shTs. Magn. Reson.  
589 Med. 89, 396–410. doi:[10.1002/mrm.29398](#).
- 590 Tournier, J.D., Smith, R., Raffelt, D., Tabbara, R., Dhollander, T., Pietsch,  
591 M., Christiaens, D., Jeurissen, B., Yeh, C.H., Connelly, A., 2019. MRtrix3:

- 592 A fast, flexible and open software framework for medical image processing  
593 and visualisation. NeuroImage 202, 116137. doi:<https://doi.org/10.1016/j.neuroimage.2019.116137>.
- 595 Trzasko, J., Manduca, A., 2011. Local versus global low-rank promotion in  
596 dynamic MRI series reconstruction, in: Proceedings of the 19th Annual  
597 Meeting of ISMRM, Montréal, CAN, p. 4371.
- 598 Tuch, D.S., Reese, T.G., Wiegell, M.R., Makris, N., Belliveau, J.W., Wedeen,  
599 V.J., 2002. High angular resolution diffusion imaging reveals intravoxel  
600 white matter fiber heterogeneity. Magn. Reson. Med. 48, 577–582. doi:[10.1002/mrm.10268](https://doi.org/10.1002/mrm.10268).
- 601
- 602 Uecker, M., Lai, P., Murphy, M.J., Virtue, P., Elad, M., Pauly, J.M.,  
603 Vasanawala, S.S., Lustig, M., 2014. ESPIRiT – an eigenvalue approach  
604 to autocalibrating parallel MRI: Where SENSE meets GRAPPA. Magn.  
605 Reson. Med. 71, 990–1001. doi:[10.1002/mrm.24751](https://doi.org/10.1002/mrm.24751).
- 606 Wu, W., Koopmans, P.J., Andersson, J.L., Miller, K.L., 2019. Diffusion  
607 Acceleration with Gaussian process Estimated Reconstruction (DAGER).  
608 Magn. Reson. Med. 82, 107–125. doi:[10.1002/mrm.27699](https://doi.org/10.1002/mrm.27699).
- 609 Wu, W., Miller, K.L., 2017. Image formation in diffusion MRI: A review  
610 of recent technical developments. J. Magn. Reson. Imaging 46, 646–662.  
611 doi:[10.1002/jmri.25664](https://doi.org/10.1002/jmri.25664).
- 612 Zhang, T., Pauly, J.M., Levesque, I.R., 2015. Accelerated parameter mapping  
613 with a locally low rank constraint. Magn. Reson. Med. 73, 655–661. doi:[10.1002/mrm.25161](https://doi.org/10.1002/mrm.25161).
- 614